1. Large Helical Device (LHD) Project

The Large Helical Device (LHD) project conducts fusion-grade confinement research in a steady-state machine and elucidates important research issues in physics and engineering for the helical-type fusion reactor.
The LHD is one of the largest superconducting helical devices, with poloidal/toroidal period numbers of 2/10, and major and averaged plasma minor radius of 3.6 – 4.0 m and 0.6 m, respectively. Three negative-ion-based 180 keV neutral beam injectors (NBIs) with total heating power of ~ 16 MW are injected tangentially to generate and heat the plasma. Two positive-ion-based 40 - 50 keV NBs with total heating power of ~ 16 MW are also injected perpendicular to the plasma. Electron cyclotron resonance heating (ECH) with total heating power of ~ 5.5 MW are installed. For fueling, the LHD is equipped with four gas puff valves and two pellet injectors.

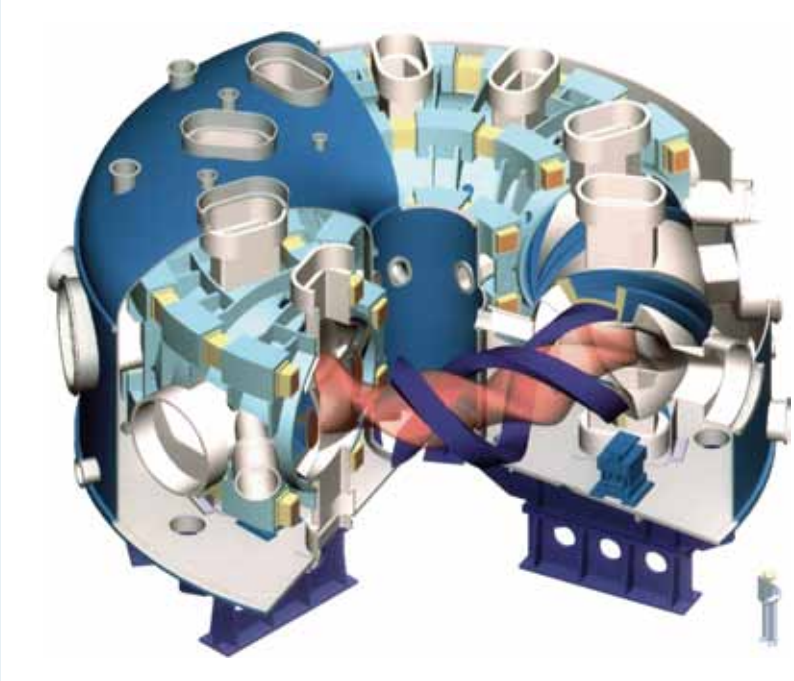

Fig. 1 The Large Helical Device (LHD). Super conducting helical coils (dark blue), poloidal coils (yellow), supporting structure (light blue) and plasma vacuum vessel (grey) are in the cryostat (blue).

In experiments conducted to date in tokamak devices, we have learned that plasma confinement performance is better in deuterium than in hydrogen. From March 2017, the LHD has begun experiments using deuterium. For the deuterium experiment, we have modified NBIs to be optimized for deuterium, and have installed new diagnostics which are mainly for the neutron, γ-ray, and high energy particle detections, as shown in Fig. 2.

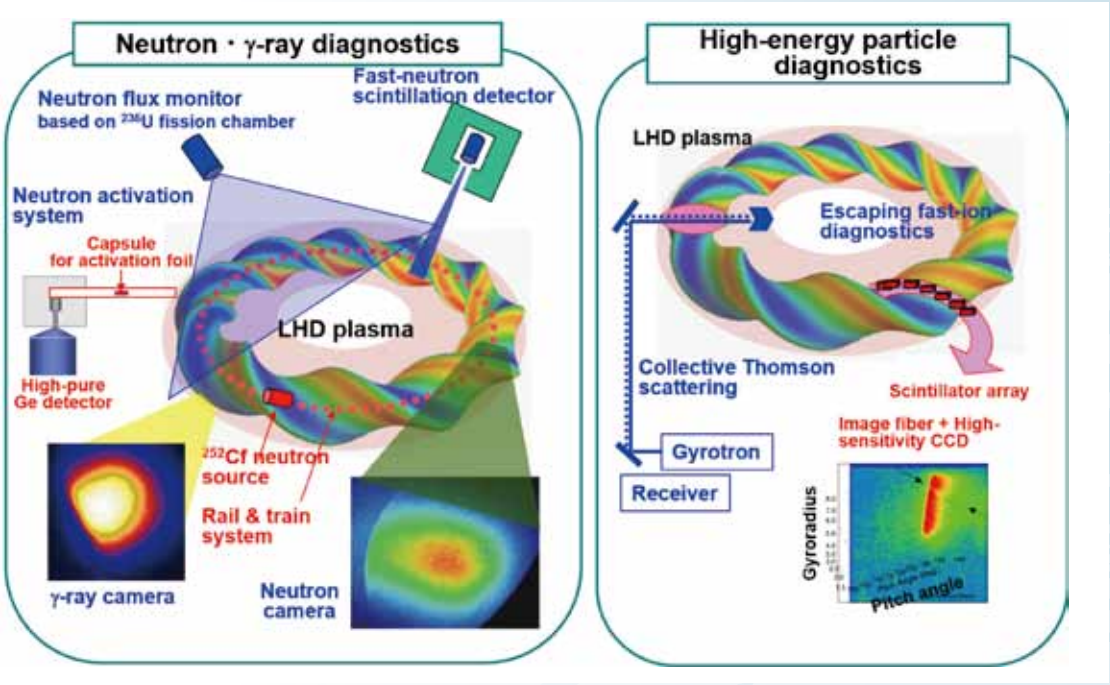

Fig. 2 Newly installed diagnostics for deuterium experiment

We do not yet understand clearly why plasma performance increases when we change the gas from hydrogen to deuterium. Clarifying the mechanism of this phenomenon, which is called the "isotope effect," also will be of great academic significance. In this project, together with experiment research using the LHD, we also will advance large-scale theoretical and simulation research that utilizes the supercomputer as the two wheels for driving fusion research forward.

Finally, achieved plasma parameters with hydrogen (before the deuterium experiment) are summarized in Table 1 with the targets of the LHD project.

Table 1 Achieved plasma parameters in hydrogen experiment (1998 - 2015).

Plasma parameters	Achieved	Target
Ion temperature	8.1 keV ($n_e = 1\times10^{19}$m^{-3})	10 keV ($n_e = 2\times10^{19}$m^{-3})
Electron temperature	20 keV (2×10^{18}m^{-3}) 10 keV (1.6×10^{19}m^{-3})	10 keV (2×10^{19}m^{-3})
Density	1.2×10^{21}m^{-3} ($T_e = 0.25$ keV)	4×10^{20}m^{-3} ($T_e = 1.3$ keV)
Beta	5.1% ($B_T = 0.425$ T) 4.1% (1 T)	5% ($B_T = 1$ - 2 T)
Steady-state operation	54min. 28sec (0.5MW, 1keV, 4×10^{18}m^{-3}) 47min. 30sec. (1.2MW, 2keV, 1×10^{19}m^{-3})	1 hour (3,000 kW)

1. Large Helical Device (LHD) Project

Highlight

LHD plasma performance has been extended, and preparation of neutron diagnostics for deuterium experiment has progressed

Simultaneous high ion temperature (T_i) and high electron temperature (T_e) regime was successfully extended by optimizing the heating scenario. Such high-temperature plasmas were realized by the simultaneous formation of an electron ITB (e-ITB) and an ion ITB (i-ITB) by the combination of high power NBI and ECRH. The ion thermal confinement was degraded in the plasma core with increase of T_e/T_i by the on-axis ECRH. In contrast, the ion thermal confinement was found to be improved at the plasma edge [1].

High-beta plasma with more than 4% was successfully produced by multi-pellet injections in one order lower collisional regime than that of previous high-beta operations. An improvement of particle confinement was observed during a high-beta discharge produced by gas-puffing, and then particle flux to divertor was reduced by more than 40%. Strong instabilities at plasma edge appeared then and suppressed an increment of averaged beta to 3.4%. Spontaneous change of the magnetic topology contributes to the increase in averaged beta value, while it triggers excitation of edge MHD instabilities [2].

Neutron flux monitor (NFM) composed of fission chambers and ^{3}He/^{10}B counters is one of the key diagnostics for LHD deuterium plasma experiment, for not only the device safety but also evaluating the plasma performance [3,4]. To obtain the total neutron emission rate/amount from the plasma by using the NFM signal, in situ calibrations of the NFM were performed, from 7 to 18 Nov. 2016, along the standard guideline on the neutron calibration technique [5].

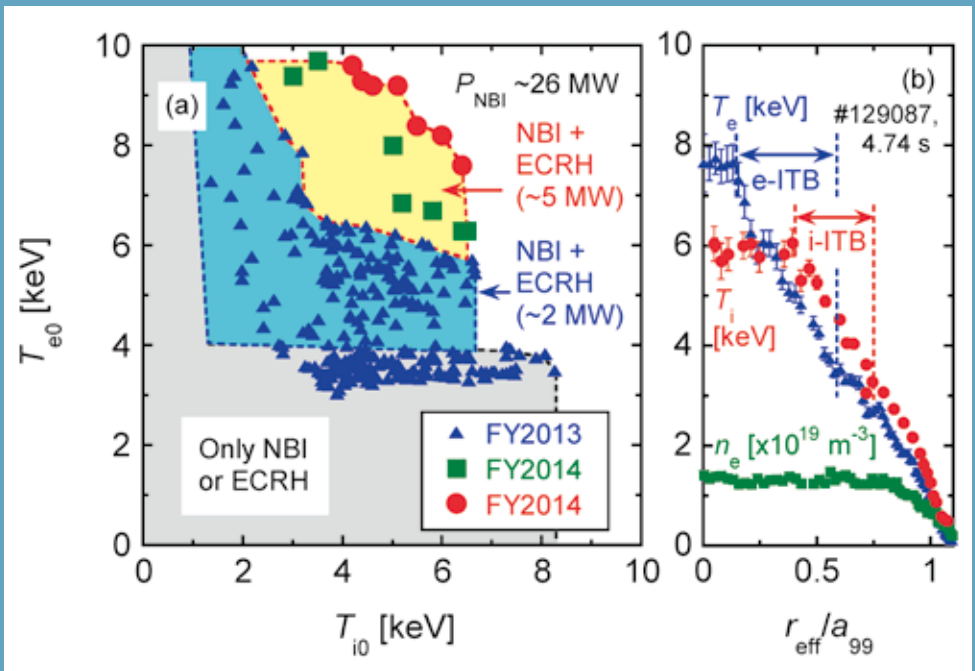

Fig. 1 (a) Extended operational high-temperature regime in the LHD, (b) T_i, T_e, and ne profiles for a typical high-temperature plasma with the ITBs. (Reproduced from Figure 2 of Ref. [1])

Extension of High-Temperature regime

In recent years, an integration of high T_i and high T_e with the simultaneous formation of an i-ITB and an e-ITB has been successfully achieved in the LHD by the combination of NBI and ECRH [6]. In FY2014, one high power gyrotron (154 GHz, 1 MW) was newly installed, and since then 5 gyrotrons with 1-MW output power each have been under operation and the total ECRH power reached 5.4 MW. Figure 1 shows (a) the latest high-temperature operational regime in the LHD, and (b) the radial profiles of T_i, T_e, and n_e for a typical high-temperature plasma associated with the e-ITB and the i-ITB. The variable r_{eff}/a_{99} in the horizontal axis of Fig. 1 (b) is the normalized-minor radius. We finely adjusted the ECRH injection angle and the EC wave polarization taking account of the actual plasma profiles in real time [7]. The circles and the squares in Fig. 1 (a) represent the data with and without the adjustment, respectively. The operational regime was successfully extended mainly due to the upgraded ECRH system and the optimization of the ECRH injection. In the present status of the LHD, the envelope of the high-temperature operational regime illustrated in Fig. 1 (a) is determined by the heating power, in other words, by the thermal transport characteristics. The global parameters of the discharge of Fig. 1 (b) are: line-averaged $n_e = 1.2\times10^{19}$ m^{-3}, $\tau_E = 33$ ms, $<\beta> = 0.53\%$, where the kinetic energy was used for the evaluation of τ_E and $<\beta>$. Although the T_i profile was flattened in the central region due to the confinement degradation by increase in T_e/T_i, the i-ITB were maintained (actually dT_i/dr_{eff} at $r_{eff}/a_{99} = 0.6$ was 2.5 times larger than that of L mode plasma).

Simultaneous high T_i and high T_e have been obtained by the on-axis ECRH superposition on the high-T_i plasmas sustained by NBI. In such condition, a seesaw-like behavior of the ion thermal transport between core and edge has been observed. In order to obtain high performance plasmas, the investigation of the ion thermal transport under the ECRH heating and the temperature profile control are important [6]. Figure 2 shows the time evolution of (a) the port through power of NBI and ECRH, (b) the kinetic energy for electron and ion, (c), (d) the gradient of T_e and T_i at $r_{eff}/a_{99} = 0.31$ and 0.98, and (e) the T_i profiles with and without ECRH. On-axis ECRH was superposed stepwise up to ~5 MW on the NBI-sustained plasma. The ray trace calculation showed that more than 90% of ECRH power was deposited inside $r_{eff}/a_{99} = 0.2$ at 4.74 s. Both in the plasma core and the edge, T_e and the gradient increased with increase of ECRH power. On the other hand, the gradient of T_i was degraded in the plasma core with increase in the ECRH power. In contrast, the T_i gradient was improved at the plasma edge. We confirmed that the ion heating power of the NBI increased during ECRH superposition because

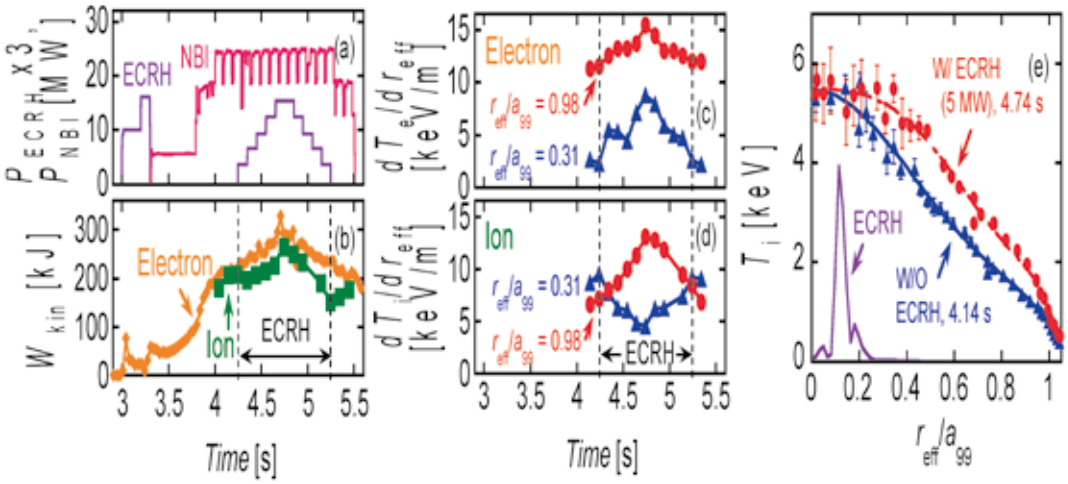

Fig. 2 Effect of ECRH on the electron- and ion-thermal confinement. The time evolution of (a) the port through power of NBI and ECRH, (b) the kinetic energy for electron and ion, (c), (d) the gradient of T_e and T_i at $r_{eff}/a_{99} = 0.31$ and 0.98, and (e) the T_i profiles with and without ECRH. (Reproduced from Figures 2 and 3 of Ref. [1])

of the increase in the beam critical energy by T_e increase. However, the increment of the ion heating power was 11% from the comparison between t = 4.24 s and 4.74 s, and this cannot explain the doubled dT_i/dr_{eff} at the edge. This edge gradient increase is considered to be a different phenomenon from the so-called confinement transition because the edge gradient changed linearly with the stepped-increased ECRH power. The normalized ion thermal diffusivity $\chi_i/T_i^{1.5}$ at r_{eff}/a_{99} = 0.98 reduced by 70%. The improvement of the ion thermal transport at the edge led to the increase in T_i in whole plasma region and the increase in the ion kinetic energy even the core ion thermal transport was degraded.

Figure 3 shows the spatiotemporal structure of the cross-correlation function of the edge n_e fluctuations at (a) 4.2 ± 0.05 s, and (b) 4.8 ± 0.05 s, and (c) the dependence of the spatiotemporal coherence of n_e fluctuations on the ECRH power. These data were obtained for the discharge introduced in Fig. 2. As can be seen from the figure, the radial structure of the edge turbulence was segmentalized by the on-axis ECRH superposition. This indicates that the correlation length of the turbulence decreased. Also, the spatiotemporal coherence decreased with increase in the ECRH power due to the change in the correlation length and the correlation time. These results implied that the edge turbulence transport decreased by on-axis ECRH and this led to the improvement of the edge ion thermal confinement.

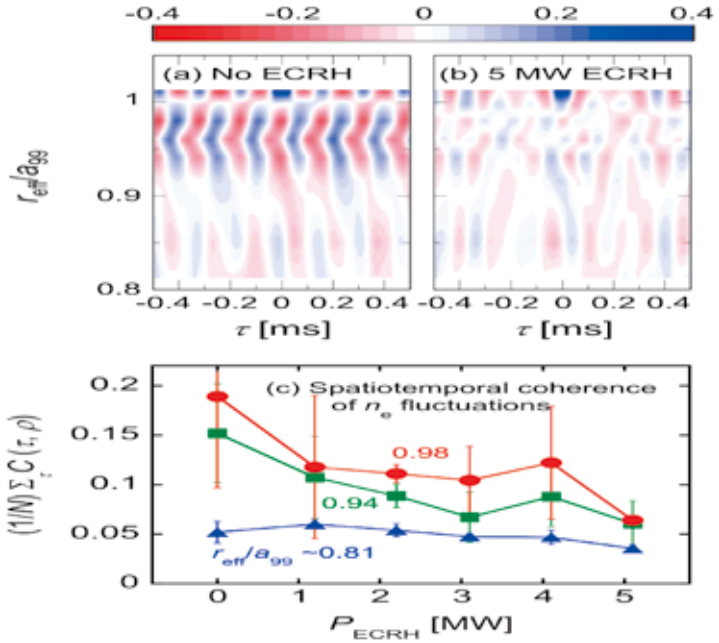

Fig. 3 Spatiotemporal structure of the cross-correlation function of the edge n_e fluctuations at (a) 4.2 ± 0.05 s, (b) 4.8 ± 0.05 s, and (c) ECRH power dependence of the spatiotemporal coherence of n_e fluctuations. (Reproduced from Figure 10 of Ref. [1])

Extension of High-beta Plasma Operation to low collisional Regime

Previous experiments in LHD show that high beta plasma with more than 5% was successfully achieved in the high collisional regime because of low magnetic field operation at 0.425 T [8]. To investigate the collisionality dependence of plasma confinement property, we have made high beta experiments in relatively high-field configurations at 1 T to increase the electron temperature. It is expected that the increase in the temperature raises magnetic Reynolds number, S, which contributes to suppression of low-n resistive interchange mode. Also recovery of plasma confinement is expected because plasma confinement in the high collisional regime (< 0.5 T) gradually decrease with beta value, which is predicted to be due to resistive-g turbulence with the same S dependence as the case of the low-n interchange mode. Also, relationship between collisionality and confinement property of high-beta plasma should be clarified from a viewpoint of characteristics of thermal /particle transport.

Figure 4 shows achieved beta value in different collisionality. In the previous high beta experiments, $<\beta>$ of 5.1% was obtained in the plasmas with ν_h^* ~ 1000 at 0.425 T. FY2014 experiments had been done at 1 T, and the optimum magnetic configuration for high-beta plasma production was explored. Consequently, $<\beta>$ of 4.1% was achieved in the plasma with T_{e0} ~ 0.9 keV and ν_h^* ~ 100 produced by the multi-pellet injections, and $<\beta>$ ~ 3.4% and ν_h^* ~ 20 were realized by gas-puff. T_{e0} reached 1.2 keV then. In the $<\beta>$ = 4.1% discharge, peaked plasma pressure is formed after the pellet injection, which causes large Shafranov shift and core instability, whereas no confinement degradation is observed then.

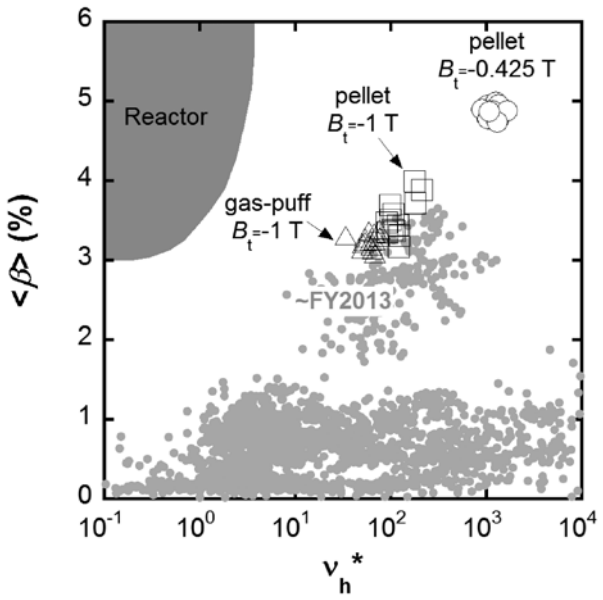

Fig. 4 Changes in achieved beta value as a function of collisionality (Reproduced from Figure 1 of Ref. [2])

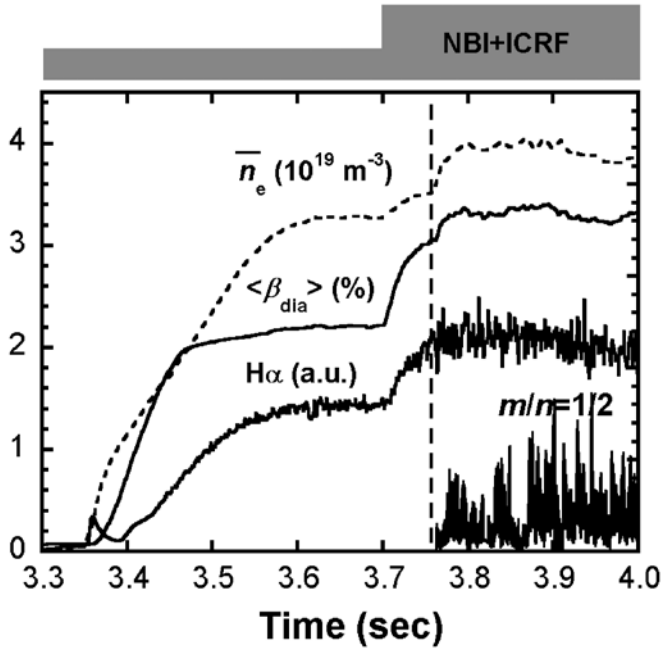

Fig. 5 Time evolutions of electron density, averaged beta, H_α and amplitude of m/n = 1/2 mode in the gas-puff discharge (Shot#129303). (Reproduced from Figure 5 of Ref. [2])

The high-beta discharges with more than 3% due to the gas-puff fueling were realized by improvement of particle confinement in peripheral region of plasma. This improvement is unclear in the pellet discharge because of short duration of high beta state (< 0.1 s). Figure 5 shows typical gas-puff discharge. The tangential NBIs produced and maintained the plasma from 3.3 s. The perpendicular NBIs and ICRF were additionally applied from 3.7 s. The electron density spontaneously increased at 3.76 s, which is due to the increment of peripheral electron density (we define this the transition here). The $<\beta>$ reached 3.4% at 3.8 s, whereas it was limited by edge MHD instabilities (m/n = 1/2).

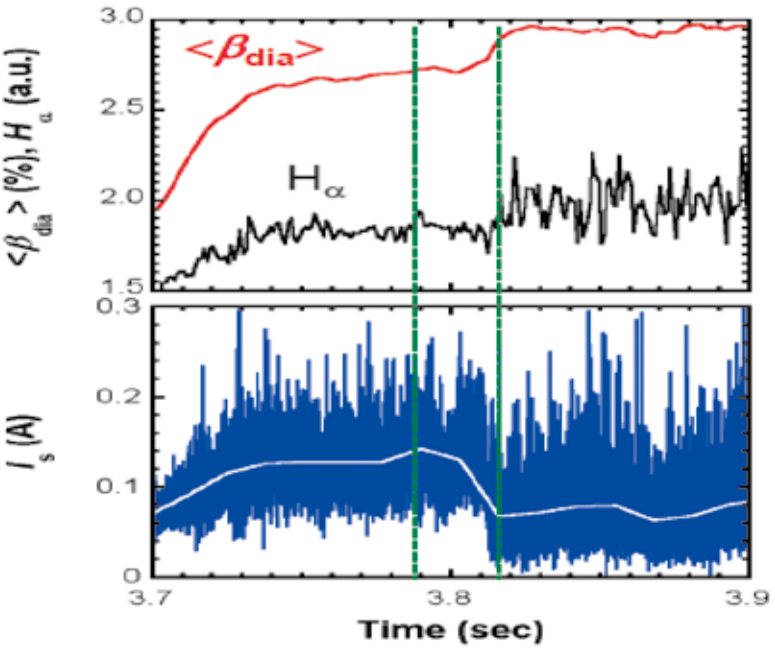

Fig. 6 Time evolutions of (a) averaged beta, H_α and (b) ion saturation current in the gas-puff discharge (Shot#130541) (Reproduced from Figure 10 of Ref. [2]).

When $<\beta>$ spontaneously increases, ion saturation current on the divertor plate was largely reduced after the transition (Fig. 6). The H_α started to decrease at 3.79 s as well as ion saturation current, and $<\beta>$ started to increase at 3.8 s. The electron density and temperature on the divertor plate also decreased then.

The m/n = 2/3 and/or 1/2 modes excited in the plasma edge were enhanced after the transition, which limit the achieved beta value. Figure 7 shows profiles of plasma pressure, rotational transform and connection length of

magnetic field line before and after the transition, which was calculated by using HINT2 code. After the transition, pressure profile was radially spread and the connection length was increased at $R > 4.57$ m. It suggests that enhancement of edge MHD instabilities are due to spontaneous appearance of rational surface with sufficiently long connection length, which means that magnetic field structure is changed from stochastic to nested one and it leads to the extension of plasma confinement region. One possibility is that the stochastic magnetic field formed by high-n magnetic islands is healed by effects of beta, collisionality and so on [9].

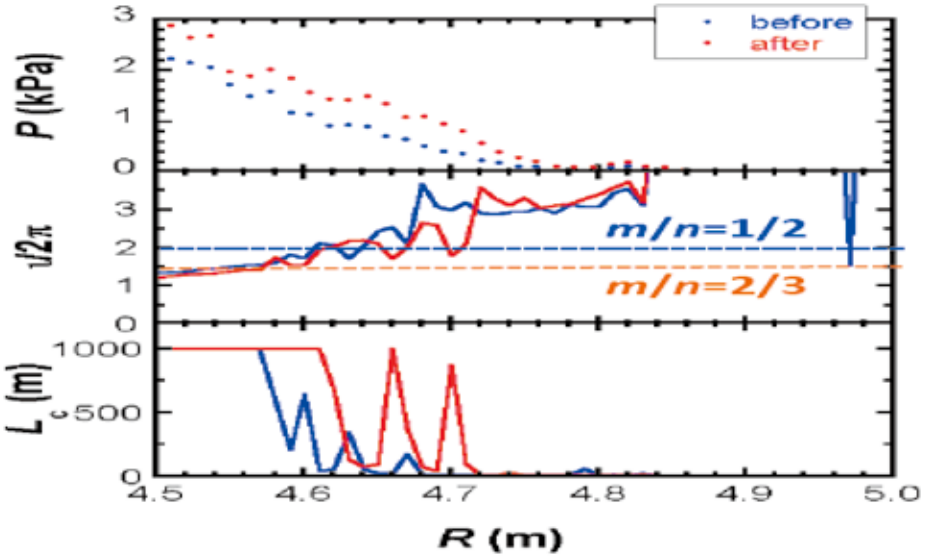

Fig. 7 Profiles of (a) electron pressure, (b) rotational transform and (c) connection length of magnetic field line before and after transition (Shot#129303, 3.73 s (before) and 3.76 s (after)) (Reproduced from Figure 8 of Ref. [2]).

Preparation of neutron diagnostics for deuterium operation

In situ calibrations of the NFM were performed from 7 to 18 Nov. 2016. We took out the absolutely calibrated neutron source from the storage container and then we loaded the neutron source on a model train. On the handling of the neutron source, we prepared a handling jig equipped with an electromagnet so as to transfer the source with keeping the distance from the source to the operator (Fig. 8). Then, we acquired neutron counts of the NFM every 0.1 s while the train runs on the ring-shaped rail track installed in the vacuum vessel along the magnetic axis position (Fig. 9). We monitored whether the train runs continuously using web cameras and a lap counter, 24 hours a day. We obtained neutron counts with changing the discrimination level of fission chamber by several steps. The calibration factor for each detector was obtained from the total counts of the NFM and the neutron emission amount from the neutron source. Point measurement was also performed to compare the numerical calculation result by means of three-dimensional neutron transport calculation code MCNP6 [10] using LHD model based on CAD drawing with some simplifications. The neutron counting rate predicted by the calculation agreed with that in experiment within a difference of several percent. We also performed in

Fig. 8 Installation of the absolutely calibrated neutron source for in-situ calibration of NFM.

situ calibration of the neutron detector for each neutral beam injector. The remote operation unit composed of a winding machine, web cameras, and a radio receiver was made to put the neutron source near the beam dump with remote controlling. Finally, the spatial resolution of the vertical neutron cameras was evaluated. We placed the neutron source at two positions by turn; the first position is just on the cylindrical collimator axis, and the second position is in the middle of two neighboring collimator axes. We found that the cross talk of the vertical neutron camera from the adjoin channel is less than one percent as predicted by the MCNP6 calculation using precise models of LHD and the vertical neutron camera. Hence, the neutron diagnostics was ready for deuterium plasma experiments on LHD.

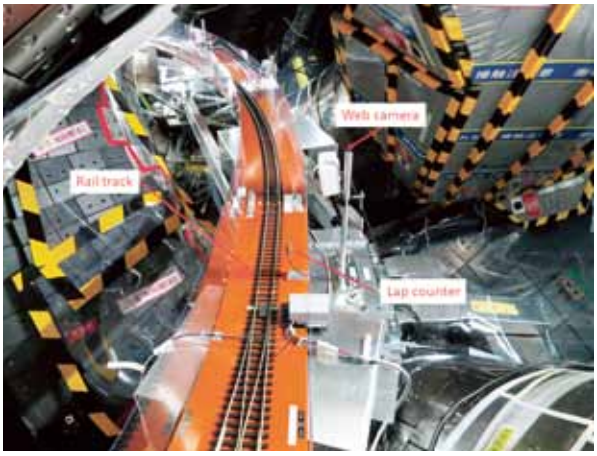

Fig. 9 Ring-shaped rail track in the vacuum vessel, and web cameras and a lap counter for in-situ calibration of NFM.

[1] H. Takahashi *et al.*, presented at 26th IAEA Fusion Energy Conference (Kyoto, 2016), PPC/1-1, and accepted for publication in Nucl. Fusion (2017).
[2] S. Sakakibara *et al.*, presented at 26th IAEA Fusion Energy Conference (Kyoto, 2016), EX/4-4, and Nucl. Fusion **57** (2017) 066007.
[3] M. Osakabe *et al.*, accepted for publication in Fusion Science and Technology (2017).
[4] M. Isobe, *et al.*, submitted to IEEE Transactions on Plasma Science (2017).
[5] J. Strachan *et al.*, Review of Scientific Instruments **61** (1990) 3501.
[6] K. Nagaoka *et al.*, Nucl. Fusion **55** (2015) 113020.
[7] T. Ii Tsujimura *et al.*, Nucl. Fusion **55** (2015) 123019.
[8] S. Sakakibara *et al.*, Plasma Phys. Control. Fusion **50** (2008) 124014.
[9] S. Sakakibara *et al.*, Plasma Phys. Control. Fusion **55** (2013) 014014.
[10] J.T. Goorley *et al.*, Los Alamos National Laboratory, LA-UR-13-22934 (2013).

1. Large Helical Device (LHD) Project

Highlight

Suppression of Impurity accumulation

Impurity accumulation is one of the import issues in order to prevent the limit of operational regime of the steady state discharge in LHD. In the past results, impurity was accumulated and introduced at particular collisionality windows [1]. In the resent results, increase of the heating power of neutral beam injection successfully prevented the impurity accumulation and the operational regime was extended [2].

Figure 1 shows density and temperature diagram of impurity behavior at the last closed flux surface. Impurity accumulation was studied from the fully ionized carbon, which intrinsically comes from sputtering at divertor carbon plate. The dashed line indicates constant ion-ion collisionality, which corresponds to identical the radial electric field. Higher than the dashed line, impurity does not accumulate due to the negative radial electric field due to the neoclassical Er effects. The plain line indicates the constant ion-ion collisionality, where the friction force in the edge ergodic layer plays significant role. Lower than the plain line, the intrinsic carbon impurity does not penetrate to the main plasma due to the effect of friction force in the ergodic layer. With the lower heating power (P_{nbi}<10MW), the data between two lines (blue colored symbol) accumulated. However, with increase of the heating power ((P_{nbi}>13MW), the data between two lines (red blank symbol in the shaded region), did not show any impurity accumulation.

The suppression of the impurity accumulation becomes more evident with increase of the normalized ion temperature gradient, toroidal Mach number, and normalized toroidal rotation gradient. Presently, the neoclassical theory without external toroidal torque does not account for the experimental observations. The effects of the toroidal torque should be considered. Also, effects of the turbulence is under investigation from the gyro-kinetic simulation.

The suppression of the impurity accumulation was also demonstrated by using electron cyclotron heating [3].

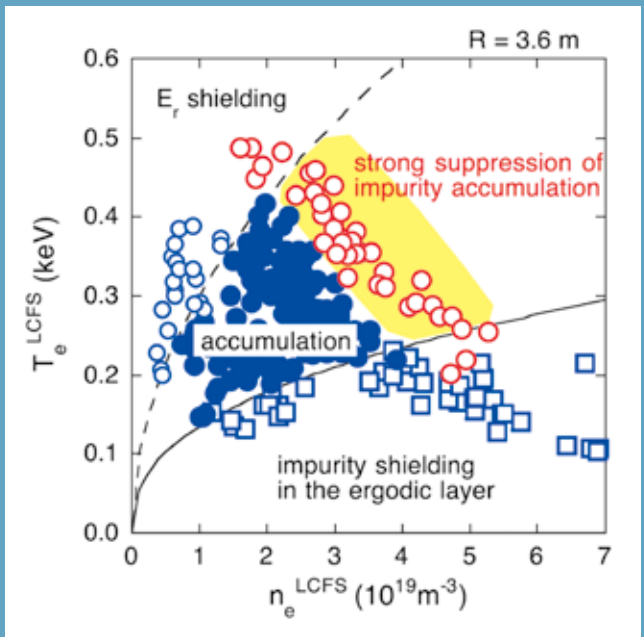

Fig. 1 n_{LCFS}-T_{LCFS} diagram of the impurity behavior. The blue symbols indicate the discharges (P_{nbi} < 10 MW) with and without impurity accumulation. The open red points represent the discharges with the strong suppression of impurity accumulation (P_{nbi} = 13 MW). Bulk ion is hydrogen.

Abruptly GAM excitation caused by the subcritical instability

New excitation mechanism of the geodesic acoustic mode (GAM) was discovered [3] and is found to be a nonlinear destabilization of a subcritical mode.

Particles and heat transport in magnetized fusion plasmas are strongly affected by turbulence and understanding the behavior of fluctuations in plasmas is essentially important. Recent studies have clarified that the GAM, which is an oscillatory zonal flow, is excited not only by turbulence but also by energetic particles and can affect the transport of energetic particles.

Newly observed GAM is shown in Fig. 2. At first, coherent modes with frequency up-chirping from about 50 to 90 kHz appear intermittently (labeled as "EGAM" in the figure). The initial frequency, which is slightly larger than the GAM frequency determined by the plasma parameters (f_{GAM}), where $f_{\mathrm{GAM}} = (1/2\pi R)\sqrt{2(T_e + 7T_i/4)/m_i}$ ~ 42kHz and m_{i} is the ion mass, indicates that the energetic particles contribute significantly to drive the mode, and the mode is identified as an EGAM. When the frequency of the EGAM reaches around $2f_{\mathrm{GAM}}$, a secondary mode is abruptly and transiently excited, as marked by red arrows in Fig. 2(b). The frequency of the secondary mode is f_{GAM}. The secondary mode appears only when the chirping EGAM presents. Thus, it is normally stable, and the presence of the EGAM is a necessary condition for the secondary mode excitation. According to the further analyses such as a mode structure and a phase relationship, the secondary mode is found to be identified as a GAM and be excited by a nonlinear destabilization of a subcritical mode. In addition, the nonlinear simulation shows this phenomenon is driven by the cooperative collaboration of fluid nonlinearity and kinetic nonlinearity [5]. This observation strongly suggests that the nonlinear excitation mechanisms work, not only in the fluid-like interaction but also in the phase space nonlinearity.

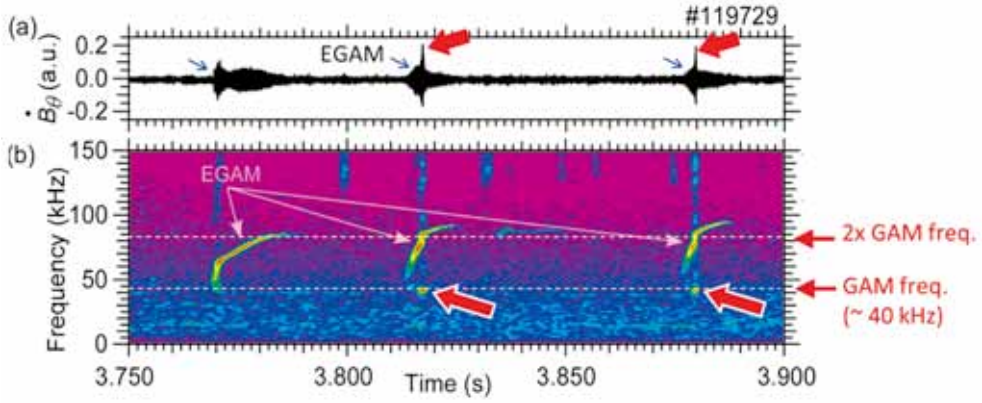

Fig. 2. (a) Typical waveform of B_θ fluctuation measured by Mirnov magnetic probe and (b) its spectrogram.

Experimental demonstration of external control of Alfven eigenmodes via ECH

Stabilization/mitigation of fast-ion-driven MHD modes via application of ECH were observed in DIII-D tokamak and TJ-II stellarator, so far. In the 19th LHD experimental campaign, it was successfully demonstrated that on axis ECH can stabilize fast-ion-driven Alfven eigenmodes (AEs). Figure 3 shows two typical discharge with different fast ion pressure profiles. In the case with peaked fast ion pressure profile (#133001), AEs with the frequency range of 250 kHz and 200 kHz disappeared when on-axis ECH was applied. The AEs with the frequency range from 50 kHz to 100 kHz were also slightly mitigated with application ECH, although low frequency MHD activities (around 10 kHz) become unstable. On the other hand, in the case with hollow fast ion pressure profile (#133010), only AE with the frequency range of 200 kHz and 300 kHz disappeared and appeared by application of on-axis ECH, respectively. To understand these differences, density profiles of counter-directed fast ions are simulated by the GNET code for the cases of #133001 and #133010. The peaked and hollow profiles of fast ions can be produced by the combination of ion source operation of counter-directed NBIs with inward shifted magnetic configuration of LHD plasmas. This means the fast ion pressure can be changed with combination of ion source operations of tangential neutral beam injectors (NBIs). These experimental observations indicate that the application of ECH is a potential candidate as an actuator for external control of fast-ion-driven AEs and the fast ion pressure profile affects both the AE excitation by fast ions and stability effects via application of ECH.

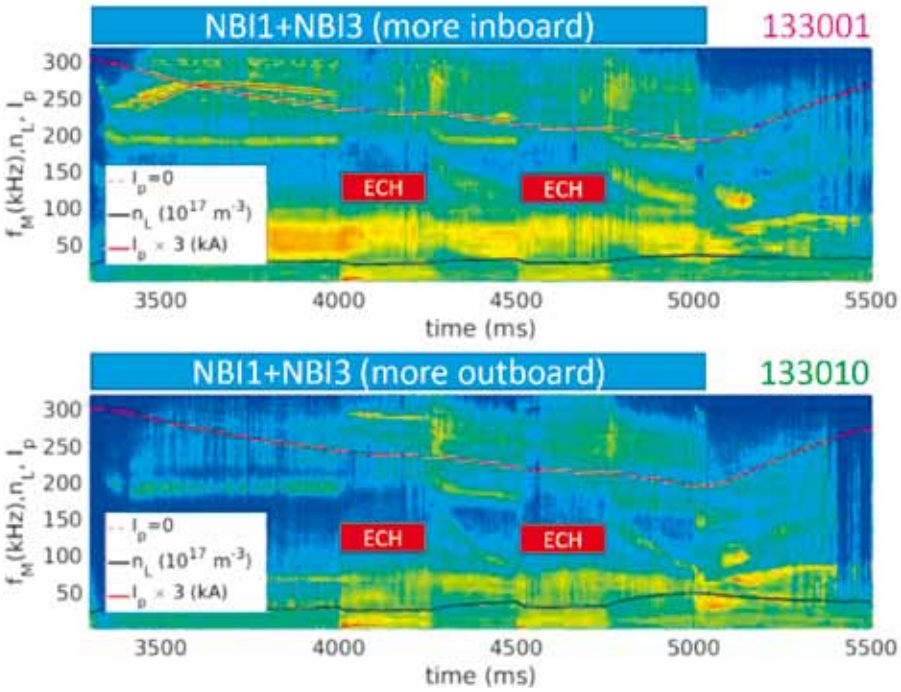

Fig. 3 Typical discharges of AE stabilization via application of ECH. On ECH injection phases, high-frequency AE activities are clearly stabilized.

The mode structure and the slowing-down mechanism of locked-mode-like instability

The locked-mode like instability, the behavior of which is similar with the locked mode in tokamaks, are observed in weak magnetic shear experiments of LHD. The features are that the mode frequency of the precursor decreases, it is finally zero (Fig. 4(g)) and the mode amplitude rapidly increases (Fig. 4(d)), which leads to the collapse (Fig. 4(a)). In order to clarify the slowing- down mechanism of the precursor, the internal structure and the slowing-down process were investigated [6, 7]. Figure 5 shows the electron temperature and its fluctuation amplitude and the phase measured by the Thomson scattering system and ECE, the shape of the amplitude and the phase during the precursor slowing-down phase suggests that the precursor has the magnetic island structure. Figure 4(e) shows the poloidal plasma flow velocity measured by the microwave Doppler reflectometers at the peripheral region. The value of the plasma flow crosses the zero, which also suggests the existence of the island. The solid line in Fig. 6(e) is the frequency of the precursor, which exactly same with Fig. 4(g) and the closed circles is the ExB drift frequency at the resonant surface, which shows that the precursor rotates together with the E × B rotation at the resonant surface. The contours in Fig. 6(g) are the radial profile of the E × B rotation frequency, and the closed circles denote the resonant surface locations. The slowing-down occurs in the 2 stages. In the 1st stage, the resonant surface moves to a small plasma flow region. In the 2nd stage, the plasma flow at the resonant surface itself slows down.

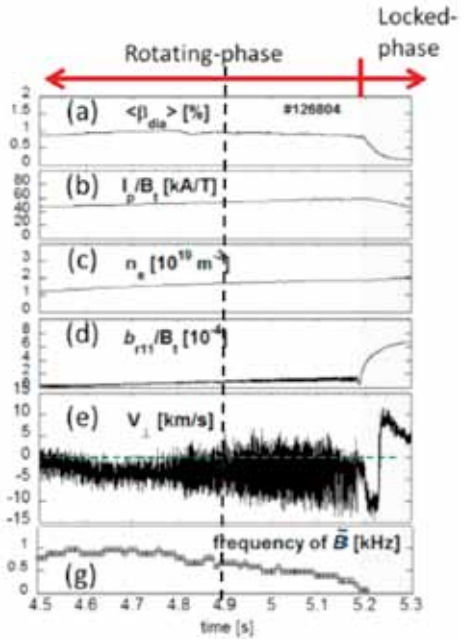

Fig. 4 Time evolutions of (a) volume-averaged beta, (b) plasma current, (c) line-averaged electron density, (d) non-rotating m/n = 1/1 fluctuation amplitude of the radial magnetic field, (e) perpendicular velocity around r/a_p = 0.9, (g) frequency of m/n = 1/1 rotating magnetic fluctuation. Cited from Fig. 1 in [6].

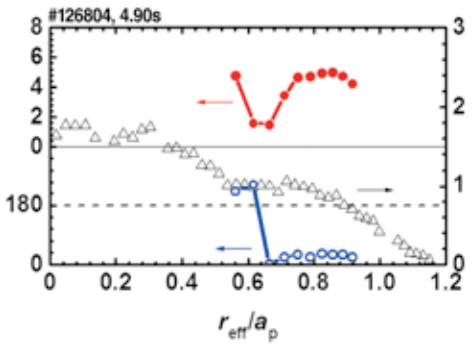

Fig. 5 Radial profiles of electron temperature and the m/n = 1/1 ECE fluctuations at 4.9s in Fig. 1. Cited from Fig. 3 in [7].

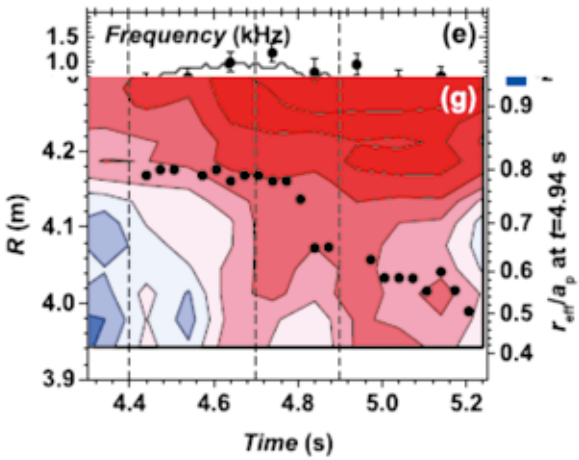

Fig. 6 (e) Frequency of the m/n = 1/1 magnetic fluctuation and the E×B rotation frequency. (g) Contours of the radial profile of the E×B rotation frequency and the resonant surface location. Cited from Fig. 2 in [7]. the resonant surface location. Cited from Fig. 2 in [2].

Observation of the ballooning type instability in the limits on the operation space of the super-dense-core plasma

In LHD, the high density plasmas with more than $1 \times 10^{21} m^{-3}$, so-called "SDC (Super-Dense-Core) plasmas", are produced by the repeatedly injected ice pellets, the central beta value of which is achieved about 10% [9]. The features of the SDC plasmas are the follows; the density gradient is much steep in the core region, which leads to the peaked pressure profile. They have the very large Shafranov shift. The so-called CDC (Core Density Collapse) phenomena are often observed, which leads to the limitation of the achieved central beta value [10]. Recently, as the precursor of CDC, we find the helical type ballooning instability at the first time in the helical plasma experiments by using an 80ch-CO_2 laser imaging interferometer system and a 2D-SX (2 Dimensional Soft X-ray) detector array system with 6x8 ch, both of which have the high special resolution. The ballooning instability appears in the negative magnetic shear region in tokamaks, and the existence was theoretically predicted only in the helical configuration [11]. Figure 7(A) shows the sight lines of the interferometer and the shapes of the magnetic flux. Figure 7(B) shows the line integrated density fluctuation amplitude by the interferometer as the function of the normalized minor radius at the equator of the torus, where the negative and the positive regions of the minor radius correspond to the torus-inside and -outside regions, respectively. This fact suggests that the mode structure is localized in a toroidal direction. In the matrixes with 6 × 8 in Fig. 7(C), the fluctuation amplitude of the SX emission is shown with the color, which suggests that the mode structure is much localized in the poloidal direction. The color contours in the Figs. 7(C) and (D) show the hypothetical mode structure drawn on the surface with the maximum fluctuation amplitude. The mode structure has the one maximum as the function of the minor radial direction, which is consistent with the two peaked structure in Fig. 7(B) as shown Fig. 7(C).

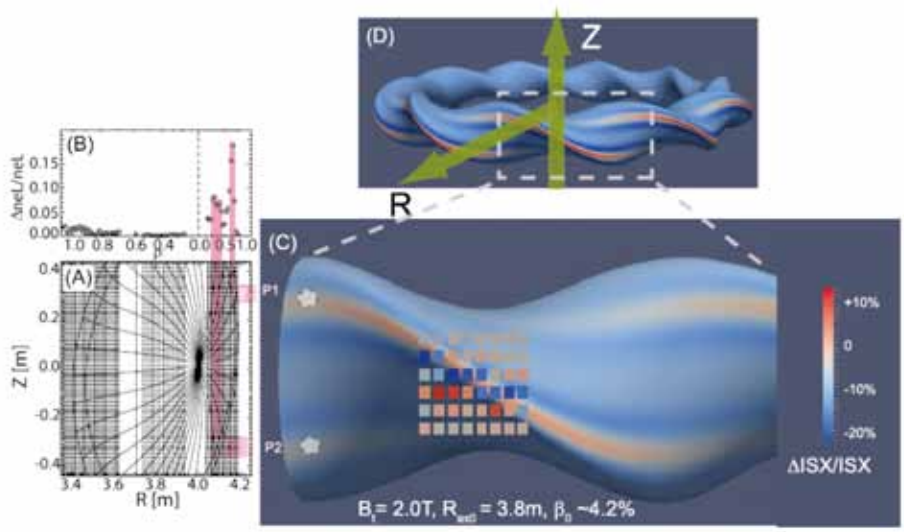

Fig. 7 (A) Sightlines of CO_2 laser imaging interferometer, (B) the line-integrated density fluctuation profile in the pre-cursor phase, (C) hypothetical mode structure drawn on the surface of a 3D image of LHD plasma ($r/a_p \sim 0.8$) together with the 2D profile of the SX emission just before the CDC. Cited from Fig. 4 in [11].

[1] Y. Nakamura *et al.*, Nucl. Fusion, **43** (2003), 219
[2] Y. Nakamura *et al.*, Nucl. Fusion, **57** (2017), 056003.
[3] N. Tamura *et al.*, Phys. Plasmas **24**, (2017), 056118
[4] T. Ido *et al.*, Phys. Rev. Lett. **116**, 015002 (2016).
[5] M. Lesur *et al.*, Phys. Rev. Lett. **116**, 015003 (2016).
[6] T.Tokuzawa *et al.*, Nucl. Fusion **57** (2017) 076003.
[7] Y.Takemura *et al.*, Plasma Fusion Res. **12** (2017) 1402028.
[8] R.Sakamoto *et al.*, Nucl. Fusion, **49** (2009) 085002.
[9] S.Ohdachi *et al.*, Contrib. Plasma Phys. **50** (2010) 552.
[10] S.Ohdachi *et al.*, Nucl. Fusion **57** (2017) 066042.
[11] N.Nakajima *et al.*, Fusion Sci. Technol. **51** (2007) 79.

Highlight

Imaging impurity emissions in the divertor/SOL region

A space-resolved visible spectroscopic system has been developed for two-dimensional (2D) distribution measurements of hydrogen and impurity emission spectra and plasma flow in the edge stochastic layer of Large Helical Device (LHD) [1]. The field of view covers entire divertor and scrape-off layer (SOL) regions, as shown in Fig. 1.

Figure 2 shows temporal evolution of edge impurity emissions of carbon during detachment transition. Carbon impurity originates from divertor plates and is main radiator in LHD. In the attached phase, t=4.60sec, emission from the C^{1+} (CII) is found to extend up to the divertor plate as shown in Fig. 2 (a). The emission from C^{2+} (CIII) is located slightly upstream of CII, i.e. away from the divertor plate. As the detachment proceeds, the emission moves upstream and literally, the plasma "detaches" from the divertor plates. Shown in the bottom line in Fig. 2 is ratio of H_γ and H_β, which is an index of volume recombination of hydrogen plasma. It is clearly observed that the ratio increases at t = 6.10 sec, around LCFS, indicating formation of very low temperature plasma at the edge region. More detailed analysis is ongoing in order to understand correlation between the emission and magnetic field structure [2].

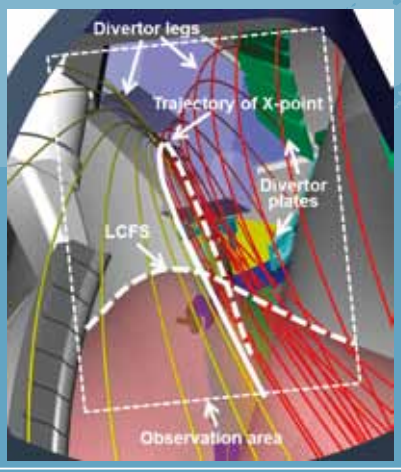

Fig. 1 Field of view of the spectroscopy system. The yellow and red lines represent divertor leg field lines, which connect to the upper and lower divertor plates. The trajectory of the X-point, the LCFS and the divertor plates are indicated. The observation area of the fiber array is shown with a rectangle. Cited from [1].

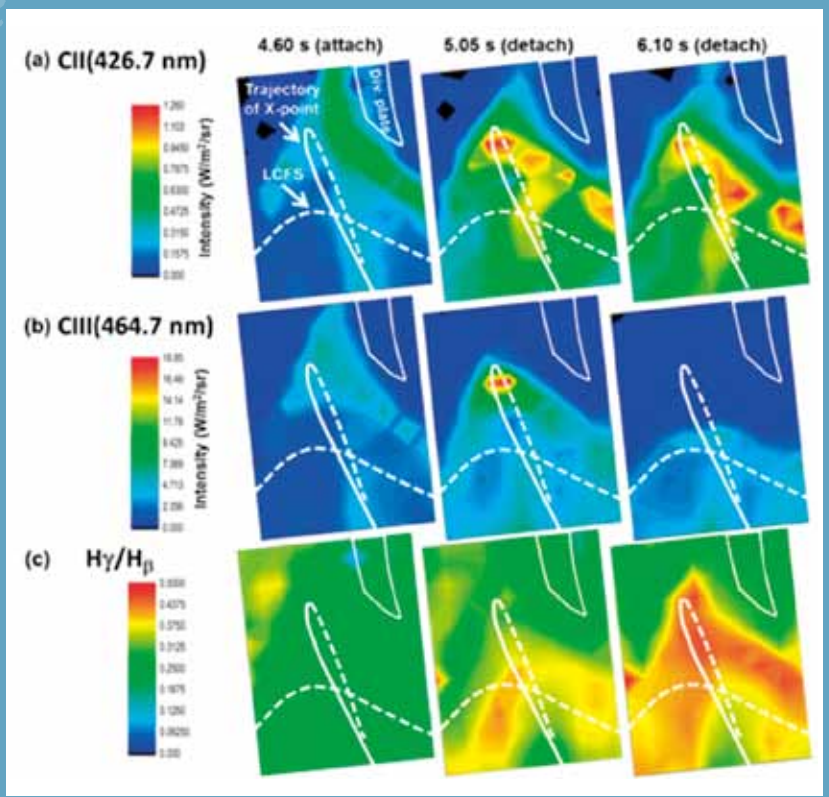

Fig. 2 2D distributions reconstructed from eission spectra. (a) CII, (b) CIII, and (c) H_γ/H_β, for the timings at t = 4.60 (attach), 5.05 (detach), and 6.10 (detach) s. The detached shot (#121345) with the RMP application. The locations of the divertor plates, the X-point trajectory, and the LCFS are indicated with the white lines.

Closed helical divertor

The control of the neutral particles using a divertor is one of critical issues in the LHD. To exploit the inherent advantage of the heliotron concept, that is the built-in helical divertor, closed helical divertor with baffle structure for high neutral particles compression has been installed at the inboard side since 2010. Moreover, to exhaust the particles highly compressed by the closed helical divertor for the density control, in-vessel cryo-sorption pumping systems inside the divertor has been installed step by step. Now, the installation of the improved cryo-sorption pumps has been completed in five sections to demonstrate its functions. Here, it is noteworthy that the development of the divertor cryo-sorption pump has progressed in NIFS.

The new pump structure was designed to maximize the conductance as shown in Fig. 3. The main characteristics is twofold: (1) The water-cooled blinds are no longer needed because the line of sight from a strike-point on the divertor plate to the LN2-cooled components is interrupted by the dome structure, and (2) the area of the cryo-sorption panel is enlarged by the integration of the cryo-sorption pump and the dome structure. To improve the performance of the cryo-sorption pump, the selection of an activated carbon is one of the key issues. In general, the activated carbon has the micro-pore and the meso-pore, whose volumes affect the pumping speed and capacity. We have examined the pumping speed and capacity of various types of the activated carbon in R&D device. Then, we found the best activated carbon and decided it as the activated carbon of the improved cryo-sorption pumps.

We conducted the pumping test of the divertor cryo-sorption pumps. The pumping speed and pumping capacity was approximately 70 m^3/s and 58,000 Pa m^3, respectively. The pumping speed is equivalent to the main vacuum pumping system of LHD, and the pumping capacity is equivalent to 20,000 hydrogen/deuterium pellets. In the 19th experimental campaign, divertor pumping effect on the LHD plasmas has been investigated.

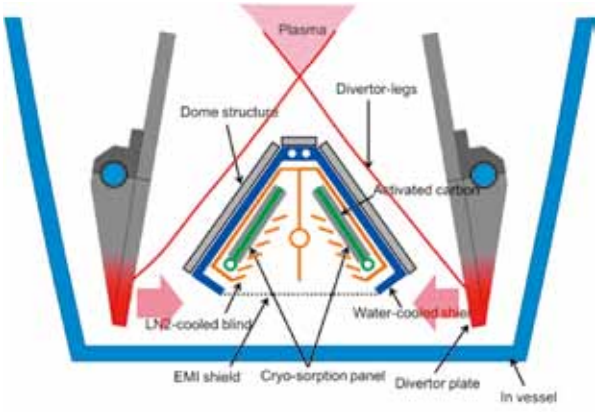

Fig. 3 Cross-section of the in-vessel new improved cryo-sorption pump.

Fig. 4 Photograph of the divertor in which the improved cryo-sorption pump is installed.

EC heating physics

In the 19th exp. campaign, so far, experiments in the plasma heating physics category such as a feedback control of EC-wave polarization corresponding to the variation of electron density, 3rd harmonic ECH, application of ECCD for high ion temperature, study of thermal equipartition between electrons and ions, study of nonlinear neutral beam-beam interaction effect, ECE measurement using ECH antenna for optimum ECH and EBWH, collective Thomson scattering measurement, were performed.

Validation of Non-Linear Collision term in FP code

A Fokker-Planck code TASK3D/FP can deal with the nonlinear neutral beam-beam interaction. When two NBIs are operated with deuterium (D) and hydrogen (H) gasses, the code predicts that the decay-time-constant of neutron yield, td, from deuterium plasmas after the stop of D-beam injection becomes longer when co-D-NBI and co-H-NBI are operated, than the case of co-D-NBI and counter-H-NBI. This prediction was qualitatively confirmed by an experiment performed in the transition phase of working gasses of the NBIs from H to D.

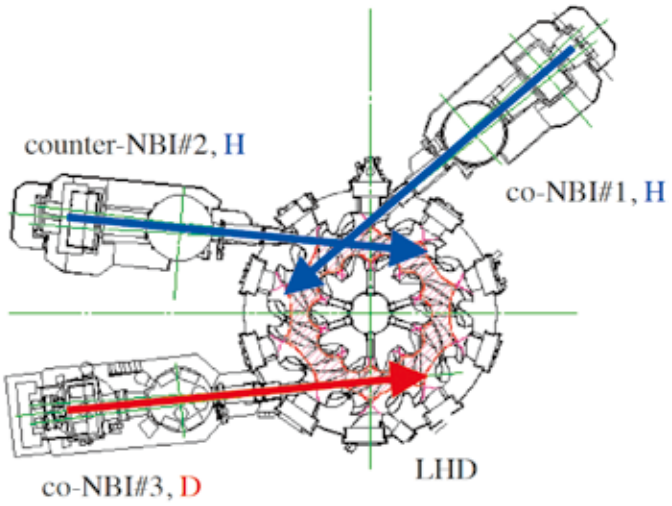

Fig. 5 Experimental setup for the confirmation of the prediction by TASK3D/FP code.

H_α measurement

Laplace inversion of the H_α line profile gives a radial distribution of the line emissivity. The result is further utilized for evaluating characteristics regarding the particle confinement.

The radial profile of particle source rate over an entire region from edge to core is derived through a detailed analysis of the H_α line profile. The results are used for evaluating the particle confinement time for a plasma volume within a magnetic flux surface, $\tau_p(r_{eff})$. Here, r_{eff} is the averaged minor radius of the flux surface and the position at $r_{eff} = 0.6$ approximately corresponds to the last closed flux surface. Characteristics of the particle confinement are evaluated in terms of $\tau_p(r_{eff})$ for different conditions of the plasma.

Figure 6 shows examples of the results for two cases. The blue curve labeled with "high β" shows the result for a discharge B_{ax} = 0.41 T, where B_{ax} is the magnetic field strength at the magnetic axis, which aims at getting the highest β value, and the red curve labeled with "high n_e" is for a discharge with B_{ax} = 2.75 T aiming at getting the highest n_e by repetitive hydrogen pellet injection. It is found that $\tau_p(r_{eff})$ in the high β discharge is significantly smaller than that in the high n_e discharge in the edge region. This result confirms that the high confinement performance for the discharges with a strong magnetic field can be ascribed, at least in part, to a high particle confinement characteristics in the plasma edge region.

The particle source rate is essential for the particle transport analysis in any fusion plasma experiment of magnetic confinement. Since the measurement only requires a simple visible observation with a line-of-sight which roughly passes through the plasma center, this technique would be applicable even for ITER and future DEMO machines where the flexibility in the observation port arrangement is considered to be extremely limited.

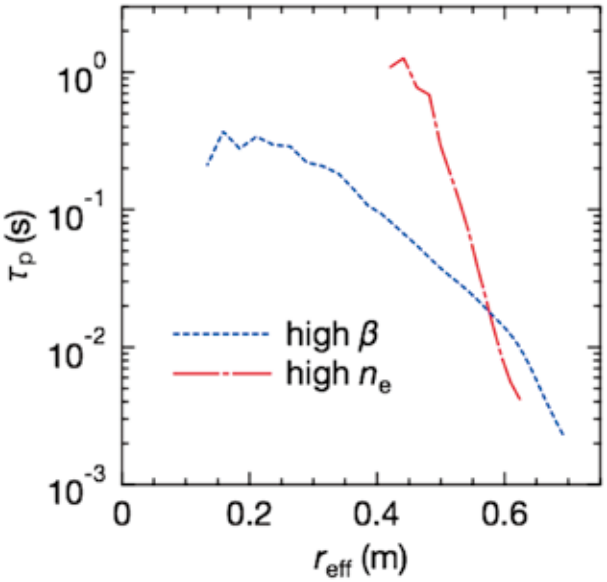

Fig. 6 Particle confinement time as a function of the magnetic flux surface represented by r_{eff} for different discharges: The dotted and dash-dotted lines show the results for the high β and high n_e plasmas, respectively (cited from [3]).

Spectroscopic study of impurity ions

Spectra from heavy ions such as tungsten, tin, lanthanides, and bismuth have been investigated by the demands of the ITER study and of a variety of plasma applications such as EUV lithography and biological microscopy. In the study of UTA (unresolved transition array) spectra in the extreme ultraviolet (EUV) wavelength region, it is found that observable spectral features drastically change between quasi-continuum radiation and discrete line radiation depending on the plasma temperature, in which some new spectral lines have been identified [4]. Figure 7 shows an example of the *Z* dependence measurements of the spectra.

The radial density distribution of W^{27+} ion has been derived from magnetic dipole (M1) line intensities in the visible wavelength range. Figure 8 shows the result of the measurement. It has been found that the tungsten concentration at plasma center is 10^{-2} at the highest and M1 line intensities can be enhanced due to proton collisions. Additionally, diffusion of tungsten ions from the plasma core is confirmed from temporal variation of the ion density profile, and poloidal asymmetry of the tungsten density distribution in the core region is inferred

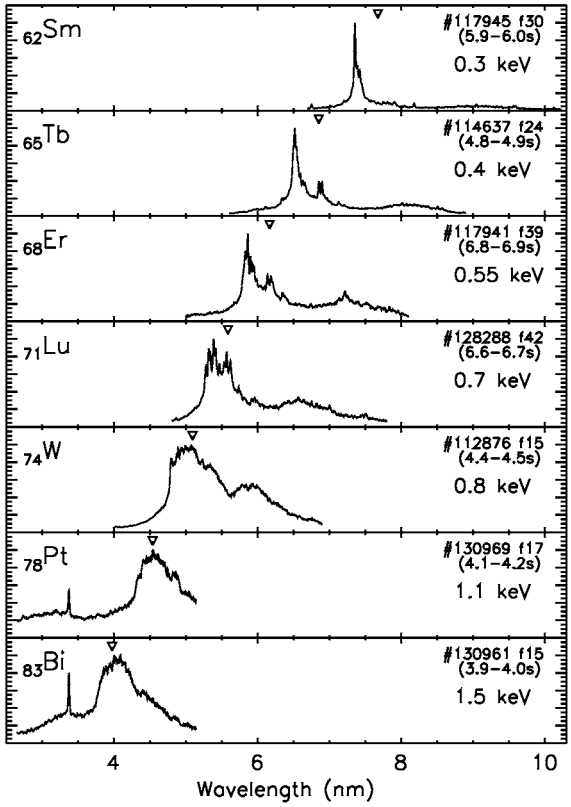

Fig. 7 *Z* dependence of the normalized EUV spectra from heavy ions with *Z* ranging from 62 to 83. The time frames were selected so that the maximum electron temperature along the line of sight is roughly equal to the ionization energies of Ag-like ions. The UTA peak positions predicted from the quasi-Moseley's law are marked by the triangles in each panel (cited from [4]).

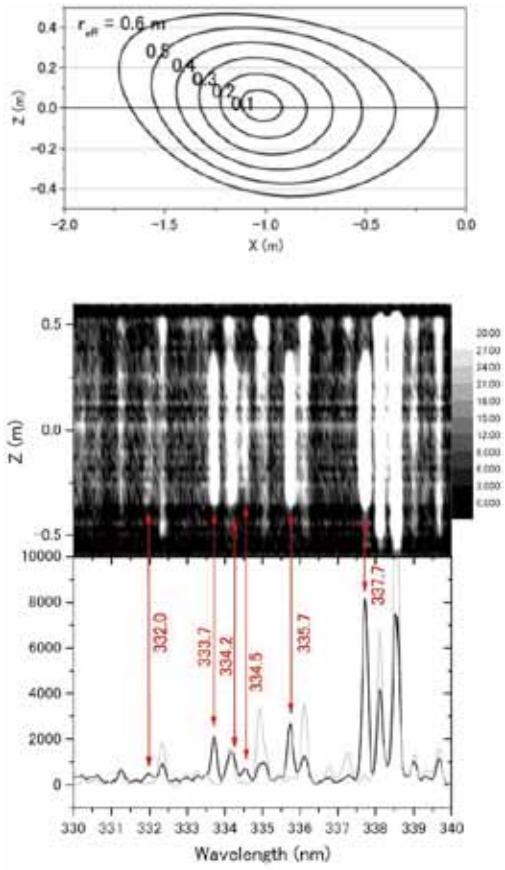

Fig. 8 Upper) Contour plot of effective minor radius r_{eff} on the poloidal cross section.
Lower) Line emission spectra in 330 – 340 nm measured at the LHD (shot No. 121534). Upper panel shows vertical profiles of line-integrated intensities. Solid indicates the spectrum measured after tungsten injection (t = 4.1 – 4.138 s), and light gray before the tungsten injection. Red arrows indicate emission lines assigned to tungsten highly charged ions. Numbers are the central wavelengths in nm (cited from [5]).

[5].

An intensive study of up-down asymmetry of tungsten ion density distribution has been made for a poloidal cross section elongated horizontally. The radial line intensity profile of a W^{27+} line has been derived from inversion of the line-integrated intensities measured with two EUV spectrometers having different wavelength ranges [6]. For the discharges analyzed so far the symmetry between in the upper half and in the lower half region looks to be preserved with high accuracy as seen in Fig. 9, which conversely indicates an availability of the present diagnostics for the asymmetry measurement.

For the RMP (resonant magnetic perturbation)-assisted detachment, the intrinsic carbon impurity is thought to play a key role. Spatial distribution of emission lines of different charge state carbon ions from C^{2+} to C^{5+} in the EUV wavelength range has been measured. The results are shown in Fig. 10. Detailed analyses of the spectral data suggest a considerable change in the magnetic field line structure in the edge region and an enhancement of impurity screening during the detachment [7]. The radiation power of C^{q+} ions with q = 2 to 5 was estimated from the intensities of resonance lines of those ions. Figure 11 shows simulation resutls for the radiation power distribution over a poloidal cross section for different charge state carbon ions. It is found that the radiation from C^{3+} ions in the ergodic layer amounts to 40% of the total radiation power loss and becomes a trigger of the detachment, whereas in the attached plasma the carbon radiation is negligibly small [8].

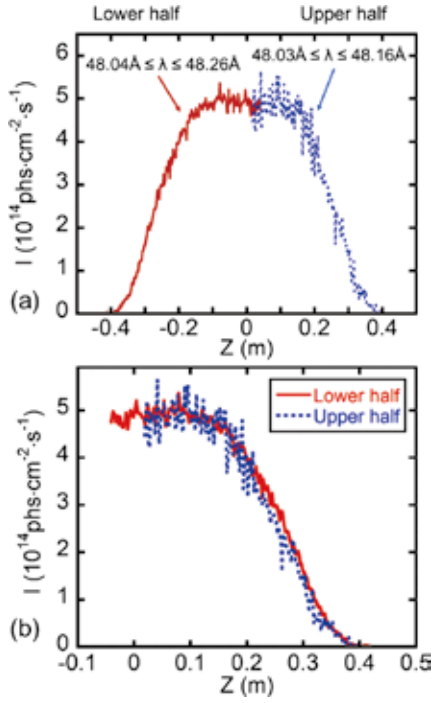

Fig. 9 (a) Vertical profiles of WXXVIII at lower- (solid line) and upper-half (dashed line) plasma radii at t = 5.3 s measured with EUV_Long2 and EUV_Short2, respectively, and (b) lower-half profile superimposed on the upper-half profile (cited from [6]).

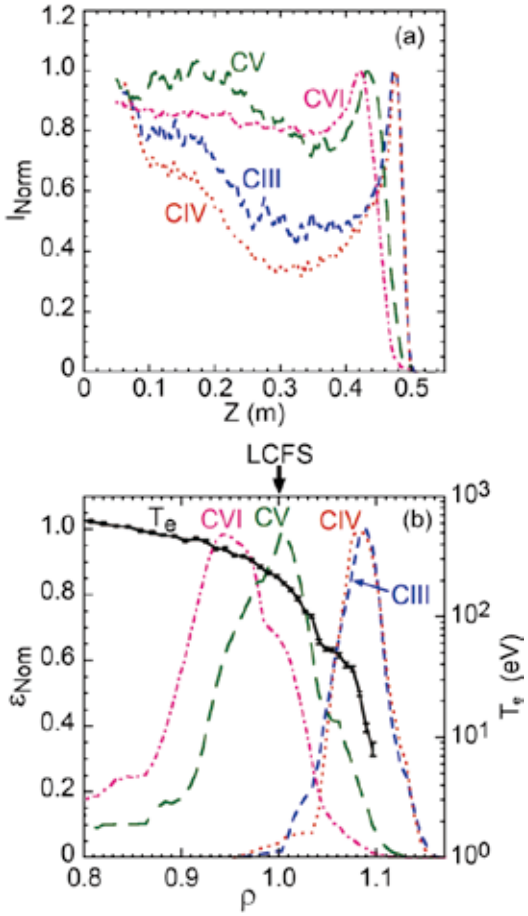

Fig. 10 (a) Normalized chord-integrated vertical profiles of CIII (38.62 nm), CIV (38.402 nm), CV (4.027 nm) and CVI (3.373 nm) and (b) normalized local emissivity profiles of CIII– CVI and T_e profile as a function of minor radius (cited from [7]).

The radial density profile measurement of iron ions for several ionization stages was performed [9]. The result shows that the iron density in the core region is smaller with a hollow electron density profile than that with a peaked density profile. A simulation code of impurity transport indicates that a transport barrier for iron ions is formed by a strong density gradient effect on the convection near the edge region when the electron density has a hollow profile. The results are shown in Fig. 12.

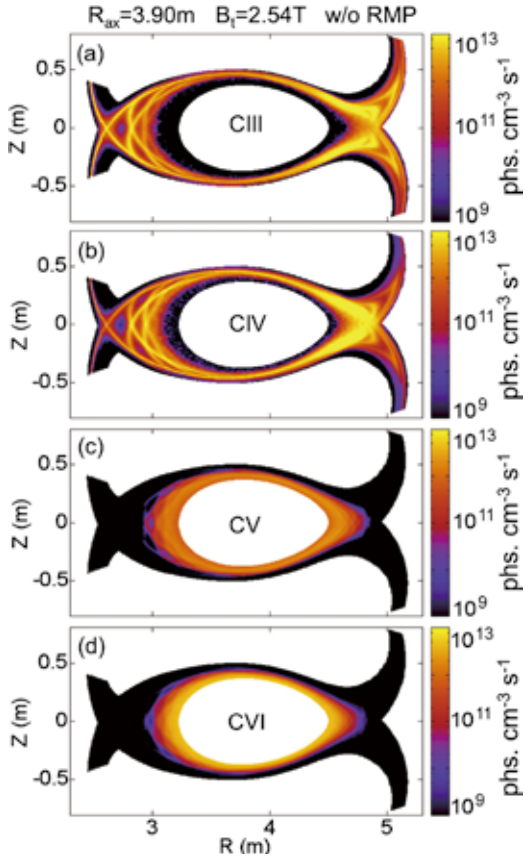

Fig. 11 Poloidal distributions of impurity emissivity in the ergodic layer simulated with EMC3-EIRENE for (a) CIII (38.6203 nm), (b) CIV (38.4174 nm), (c) CV (4.027 nm), and (d) CVI (3.373 nm) in R_{ax} = 3.90 m configuration without RMP (cited from [8]).

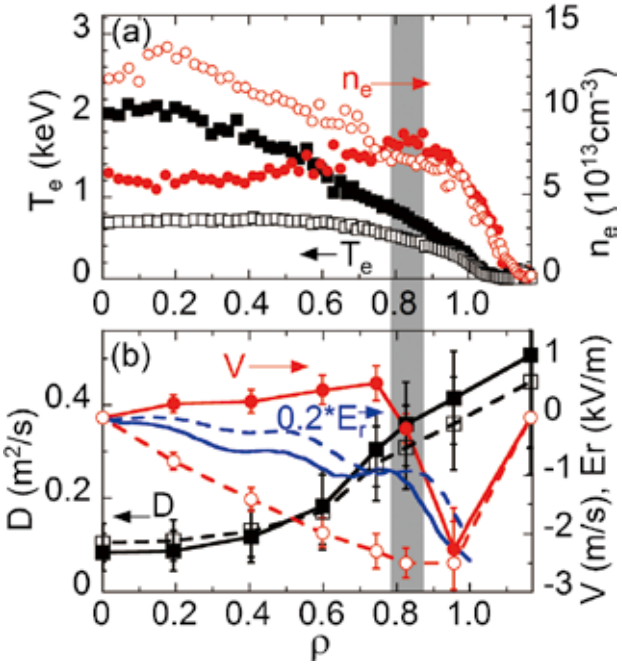

Fig. 12 Radial profiles of (a) electron temperature (squares) and density (circles) and (b) diffusion coefficient (squares), convective velocity (circles) and radial electric field for peaked (open symbols or dashed lines) and hollow (solid symbols or solid lines) ne profile discharges. Hatched area denotes radial region of impurity transport barrier (cited from [9]).

[1] M. Kobayashi *et al.*, RSI **88** (2017) 033501
[2] M. Kobayashi *et al.*, Nuclear Materials and Energy
[3] M. Goto, *et al.*, Plasma Phys. Control. Fusion **58**, 084001 (2016).
[4] C. Suzuki, *et al.*, Plasma Phys. Control. Fusion **59**, 014009 (2016).
[5] D. Kato, *et al.*, Proceedings of the 26th IAEA Fusion Energy Conference, Kyoto (2016).
[6] Y. Liu, *et al.*, Rev. Sic. Instrum. **87**, 11E308 (2016).
[7] H. Zhang, *et al.*, Plasma and Fusion Research **11**, 2402019 (2016).
[8] H. Zhang, *et al.*, Phys. Plasmas **24**, 022510 (2017).
[9] X. L. Huang, *et al.*, Nucl. Fusion, in press.

Highlight

Long-Term Reliability of LHD Superconducting Magnet Systems

IIn the LHD superconducting magnet systems (Fig. 1), numerous efforts have been made to operate the system stably and reliably over the long term for achievement of excellent results in the LHD plasma experiment. Total operating time of the LHD cryogenic system for the superconducting magnet reaches 80,000 hours and the availability exceeds 99 % due to appropriate maintenances, replacement and improvement. In August of 2016, the cooling capacity of the refrigerator/liquefier was examined and the 4.4 K equivalent cooling capacity of 9.19 kW was obtained. Consequently, it was confirmed that the cooling capacity of the helium refrigerator/liquefier was almost equivalent to that during commissioning test in 1995. In the poloidal coils, the AC losses have been monitored from the third to the eighteenth plasma experimental campaign in order to comprehend the present status. As results, it was found that the AC losses slightly decreased until the fifth campaign except for the lower inner vertical coil and have remained unchanged since then. It is considered that the initial change of the AC losses was probably caused by the decrease of inter-strand coupling losses due to the change of the contact situation between strands. In the DC current supplies, the control systems, which are control computers and both programmable logic controllers and control circuits installed in the thyristor rectifiers, have been updated since 2013. The update was completed in 2016.

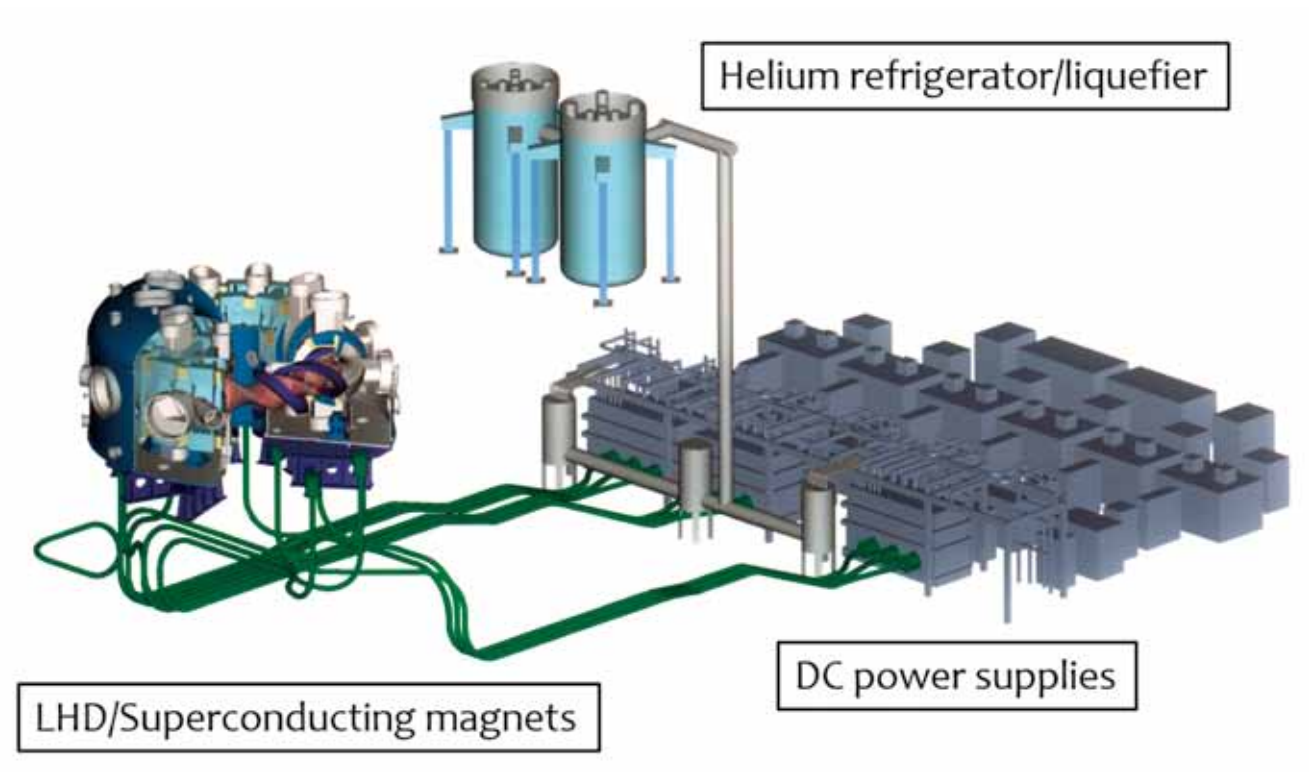

Fig. 1 Schematics of the LHD superconducting magnet systems cited from [1].

Helium Refrigerator/Liquefier

The LHD has a helium refrigerator/liquefier (Fig. 2) to cool down the superconducting magnet systems, which consists of a pair of pool-cooled helical coils, three pairs of force-cooled poloidal coils and nine superconducting bus-lines (Fig. 3). Nominal cooling capacity of the refrigerator/liquefier is the helium liquefaction rate of 650 l/h and the refrigeration power of 5.65 kW at 4.4 K and 20.6 kW at 80 K, which correspond to the 4.4 K equivalent cooling capacity of 9.1 kW. The LHD cryogenic system including the refrigerator/liquefier has been operated stably and reliably for eighteen plasma experimental campaigns due to appropriate maintenances and the total operating time was 78,170 hours. The availability exceeded 99 % and the mean time between failures (MTBF) was 2,895 hours. However, deterioration of the cooling capacity of the refrigerator/liquefier was suspected because it was observed that the pressure drop of filters increased gradually. Hence, all the filters and first stage of double column type adsorber (ADS1) were replaced after the eighteenth plasma experimental campaign.

In August of 2016, the cooling capacity of the refrigerator/liquefier was measured after the replacement. So far, such a test was only conducted once during the commissioning of the refrigerator/liquefier in June of 1995. As the result of the present test, it was obtained that the cooling capacity was the helium liquefaction rate of 606 l/h and the refrigeration power of 5.67 kW at 4.4 K and 23.35 kW at 80 K, which correspond to the 4.4 K equivalent cooling capacity of 9.19 kW. It was reduced by only 2 % from the previous test. It can be mentioned that the present cooling capacity is almost equivalent to the previous cooling capacity because there are difference of atmospheric temperature and measuring uncertainty.

Now, the cryogenic system has been operated for the nineteenth plasma experimental campaign. The schedule is as follows; (1) the purification operation periods were from Dec. 21, 2016 to Dec. 28, 2016 and from Jan. 4, 2017 to Jan. 10, 2017, (2) the cool-down operation period was from Jan. 11, 2017 to Feb. 5, 2017, (3) the steady state operation started on Feb. 6, 2017 and it is currently in process. The LHD superconducting magnet systems

Fig. 2 Photograph of helium refrigerator/liquefier for the LHD.

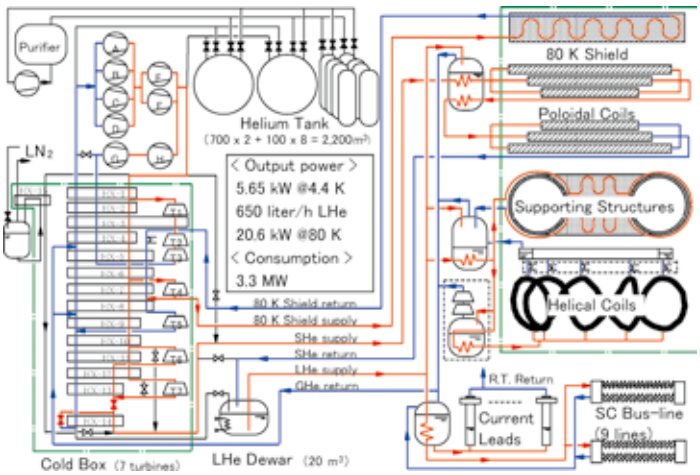

Fig. 3 Flow diagram of the LHD superconducting magnet systems cited from [1].

have been cooled down according to the above schedule. After excitation tests of the superconducting magnets were carried out for two days, hydrogen plasma experiments started on Feb. 8, 2017. Then, deuterium plasma experiments started on Mar. 7, 2017. The LHD cryogenic system with the helium refrigerator/liquefier continues working without trouble during the deuterium plasma experiments.

Poloidal Coils

The poloidal coils are wound with cable-in-conduit (CIC) conductors without sub-channels and are cooled by forced flow of supercritical helium. The coils consist of three pairs of circular coils stacked with eight double pancakes (Fig. 4, Fig. 5). The coils have experienced 50,119 hours of steady state cooling operation, 1,625 excitations and eighteen thermal cycles during eighteen plasma experimental campaigns, while super-to-normal transition has never been observed. Generally, AC losses of superconducting coils using CIC conductors include inter-strand coupling losses and the losses are changed by the contact situation between strands. It is considered that the contact situation is changed by the thermal cycles and the electromagnetic forces. So, the AC losses of the four poloidal coils, which are a pair of inner vertical (IV) coils and a pair of outer vertical (OV) coils, have been investigated from the third to the eighteenth plasma experimental campaign in order to comprehend the present status.

The inlet temperature, the outlet temperature and the mass flow rate of supercritical helium through the coils were measured after discharges of the coils, and then the AC losses were estimated by the difference between the inlet and outlet enthalpy calculated by using the measured values. As the results, the AC losses slightly decreased until the fifth campaign except for the lower IV coil and the losses have remained unchanged since then. The hysteresis and inter-filament coupling losses in the AC losses are unlikely to change because they depend on only

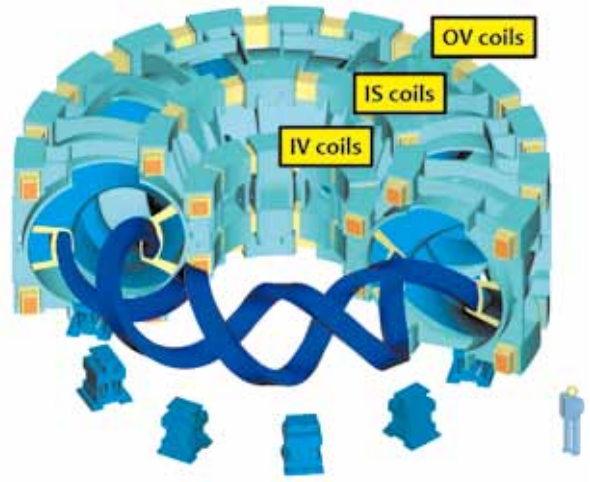

Fig. 4 Schematics of the LHD superconducting magnets.

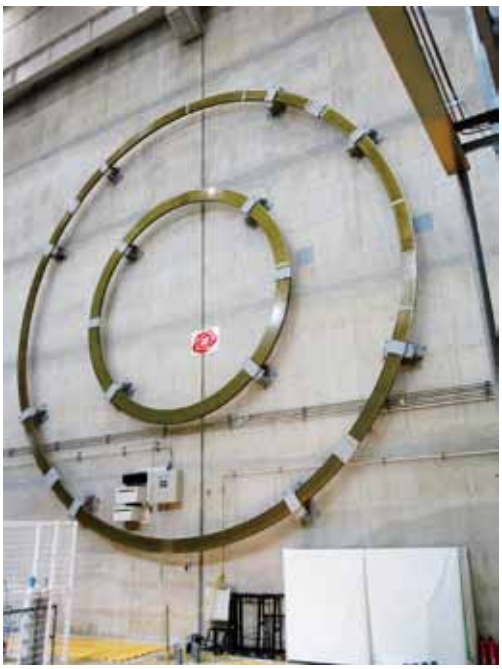

Fig. 5 Mock-ups of double pancakes for IS coil (inner side) and OV coil (outer side).

the structure of the strand. Thus, it is considered that the initial change of the AC losses was probably caused by the decrease of inter-strand coupling losses due to the change of the contact situation between strands. The strands were moved by the electromagnetic forces during excitations of the coils and then close contacts with large area, produced by plastic deformation of the strand surface during the cabling and jacketing processes, may be removed. Actually, the maximum magnetic field of the LHD had increased gradually until the fourth plasma experimental campaign for enhancement of plasma parameters. On the other hands, the coupling losses increased with increasing the excitation number in the case of the ITER poloidal field conductor insert (PFCI) because the inter-strand contact resistance decreased by compressive deformation of the cable cross-section or polishing of the strand surface. However, it is considered that the decrease of the electrical contact have not been induced in the cases of both the IV and OV coils because the maximum electromagnetic forces applied to the coils are approximately one third of those of the PFCI.

DC Power Supplies

The LHD has six DC power supplies to excite both one pair of helical coils and three pairs of poloidal coils. The control systems for the power supplies, which are control computers and both programmable logic controllers (PLCs) and control circuits installed in the thyristor rectifiers, have been continuously used after construction. Although the power system has been operated for about 20 years without severe problem, some components became overage and it became difficult to maintain them. Therefore, they have been updated for four years. The updated components are listed as follows;

(1) PLCs in 2013, (2) filter capacitors of DC main circuit in 2014, (3) communication unit for setting in 2015, (4) control computers in 2016. The real time computers were changed from VME bus system to compact PCI system and the supervisor computer was changed from Sun workstation to a Linux based workstation. At the same time, the data link with optical interface and LAN are upgraded to higher speed models.

[1] S. Imagawa *et al.*, Nucl. Fusion **47** (2007) 353-360.

(T. Morisaki)